HHS Public Access

Author manuscript

Nano Lett. Author manuscript; available in PMC 2019 April 11.

Published in final edited form as:

Nano Lett. 2018 April 11; 18(4): 2195–2208. doi:10.1021/acs.nanolett.7b04043.

Differences in Nanoparticle Uptake in Transplanted and Autochthonous Models of Pancreatic Cancer

Zhimin Tao[1,*], **Mandar Deepak Muzumdar**[1,2,3,4,*], **Alexandre Detappe**[1,2,3], **Xing Huang**[1], **Eric S. Xu**[1], **Yingjie Yu**[1], **Tarek H. Mouhieddine**[2,3], **Haiqin Song**[1], **Tyler Jacks**[1], and **P. Peter Ghoroghchian**[1,2,3,#]

[1]Koch Institute for Integrative Cancer Research at MIT, 500 Main Street, Cambridge, MA 02139, USA

[2]Dana Farber Cancer Institute, 450 Brookline Avenue, Boston, MA 02215, USA

[3]Harvard Medical School, 25 Shattuck Street, Boston, MA 02115, USA

[4]Yale University School of Medicine, 333 Cedar Street, New Haven, CT 06510, USA

Abstract

Human pancreatic ductal adenocarcinoma (PDAC) contains a distinctively dense stroma that limits the accessibility of anticancer drugs, contributing to its poor overall prognosis. Nanoparticles can enhance drug delivery and retention in pancreatic tumors and have been utilized clinically for their treatment. In preclinical studies, various mouse models differentially recapitulate the microenvironmental features of human PDAC. Here, we demonstrate that through utilization of different organic co-solvents and by doping of a homopolymer of poly(ε-caprolactone), a diblock copolymer composition of poly(ethylene oxide)-*block*-poly(ε-caprolactone) may be utilized to generate biodegradable and nanoscale micelles with different physical properties. Noninvasive optical imaging was employed to examine the pharmacology and biodistribution of these various nanoparticle formulations in both allografted and autochthonous mouse models of PDAC. In contrast to the results reported with transplanted tumors, spherical micelles as large as 300 nm in diameter were found to extravasate in the autochthonous model, reaching a distance of approximately 20 μm from the nearest tumor cell clusters. A lipophilic platinum(IV) prodrug of oxaliplatin was further able to achieve a ~7-fold higher peak accumulation and a ~50-fold increase in its retention half-life in pancreatic tumors when delivered with 100 nm-long worm-like micelles as when compared to the free drug formulation of oxaliplatin. Through further engineering of nanoparticle properties, as well as by widespread adoption of the autochthonous tumor model for preclinical testing, future therapeutic formulations may further enhance the targeting and penetration of anticancer agents to improve survival outcomes in PDAC.

[#]To whom correspondence should be addressed: P. Peter Ghoroghchian, M.D., Ph.D., Charles W. and Jennifer C. Johnson Clinical Investigator, Koch Institute for Integrative Cancer Research, Massachusetts Institute of Technology, 77 Massachusetts Avenue, 76-261F, Cambridge, MA 02139, USA, (617) 252-1163, ppg@mit.edu.

[*]Denotes equal author contribution

CONFLICTS OF INTEREST

There are no conflicts of interest to declare.

SUPPORTING INFORMATION

Supplementary Figures S1 thru S10, Scheme S1, and Supplementary References may be found in the accompanying Supporting Information.

Keywords

Drug delivery; Nanomedicine; Pancreatic ductal adenocarcinoma; Platinum(IV); Optical Imaging

Pancreatic ductal adenocarcinoma (PDAC) is the third leading cause of cancer death in the United States and a significant contributor to morbidity and mortality worldwide[1, 2]. In spite of advances in combination chemotherapy (*e.g.,* FOLFIRINOX[3] and gemcitabine/nab-paclitaxel[4]), which offer greater response rates and prolong median survival, long-term survival remains poor at 8%[1, 2]. These therapies also induce considerable adverse effects, limiting their use to patients with good performance status. Given that most patients are diagnosed with unresectable disease at the time of initial presentation[2], novel approaches for the treatment of advanced pancreatic cancers are desperately needed.

A defining feature of PDAC is the extraordinary heterogeneity of the tumor microenvironment[5–7]. Pancreatic tumor cells are surrounded by a dense stroma that possesses diverse cellular (*e.g.*, fibroblasts, macrophages, immune cells) and acellular components (*e.g.*, extracellular matrix proteins, hyaluronic acid), which together can comprise > 90% of the tumor by volume[6]. These stromal features contribute to increased interstitial pressures, impairing intratumoral blood flow and therapeutic delivery to PDAC cells. Efforts to modify the cellular (*e.g.*, through hedgehog inhibition[8]) and acellular microenvironment (*e.g.*, with the use of hyaluronidase[9, 10]) have improved vascularization and tumor responses in preclinical PDAC models; they have also shown early promise in clinical trials[11, 12]. Overcoming the stromal barrier can, thus, enhance the efficacy of existing cytotoxic chemotherapies directed against PDAC, potentially affording greater tumor responses at lower doses and with fewer systemic side effects.

Nanomedicine offers a means by which to improve anticancer drug delivery through both passive and active targeting mechanisms that promote nanoparticle accumulation in tumors[13–16]. Nanoparticles have also been successfully utilized to improve clinical outcomes in pancreatic cancers[4, 17]. Conjugation of cancer cell-specific targeting moieties to nanoparticles can potentially promote greater drug accumulation at tumor sites, minimizing side effects and maximizing therapeutic activity[18–20]. While lipid-based nanoparticles have been widely-adopted in translational research due to their outstanding biocompatibility, their labile nature may affect stability during both product storage and *in vivo* administration; polymeric nanoparticles can be better engineered for controlled biodegradability but must overcome concerns related to potential toxicity and immunogenicity.[21–26] As an example of the successful preclinical application of the latter, platinum-based anticancer agents have been incorporated into polymeric micelles to prolong their blood circulation times and to enhance tumor accumulation in transgenic as well as in transplanted models of human PDAC[27–30]. These studies have revealed the potential for nanoparticles of smaller sizes to exhibit preferential accrual in pancreatic tumors[28, 31]. Little is known, however, about the effects of other nanoparticle characteristics, such as shape, on affecting drug delivery. Moreover, the inconsistent findings reported from previous nanoparticle studies may be attributable to differences in vascular density, in the sizes of endothelial gap junctions, and in the extent of the desmoplastic stroma in the specific transgenic or transplanted tumor model

that was utilized; these key features play critical roles in disease pathogenesis, in limiting nanoparticle extravasation and parenchymal drug diffusion, and in stymying the efficacy of antitumor therapies. It is important to underscore that all transgenic and transplanted tumor models fail to faithfully recapitulate the genetic and biological characteristics of human PDAC.[8]

Genetically-engineered mouse models of pancreatic cancer have been recently developed in which tumors arise spontaneously in the mouse's own pancreas (*i.e.*, autochthonous models)[32–34]. These models accurately mimic the genetic and molecular changes that occur during the step-wise progression of human PDAC, including the development of its desmoplastic stroma[32–34]. We, therefore, utilized both subcutaneous transplant and autochthonous murine models of PDAC to systematically evaluate the interplay between different nanoparticle characteristics (*e.g.*, size and shape) and their impact on overcoming the unique features of each tumor model (*i.e.*, differences in vascular and stromal density) to augment *in vivo* delivery.

Generation of polymeric nanoparticles of varying size and shape for *in vivo* delivery

Poly(ethylene oxide)-*block*-poly(ε-caprolactone) (PEO-*b*-PCL) is an amphiphilic diblock copolymer composition comprised of two FDA-approved building blocks that impart favorable physicochemical and biological characteristics, including prolonged *in vivo* stability, enhanced aqueous solubility (imparted by the PEO block), full biodegradability (of the PCL block), and low *in vitro* or *in vivo* toxicity; moreover, while repeated administration of any PEO-coated nanoparticle may elicit a humoral immune response, PEO-*b*-PCL-based vehicles have been shown to induce minimal immunogenicity.[35] We have previously explored the phase behavior of different PEO-*b*-PCL molecular weight compositions, identifying those that readily generate nanoscale vesicles and spherical micelles in aqueous suspension[36, 37]. We have demonstrated that PEO-*b*-PCL-based vesicles can incorporate both chemotherapeutic species[36] and near-infrared (NIR) fluorophores[38]. Additionally, we have conducted *in vivo* optical imaging studies that have determined preferential accumulation of PEO-*b*-PCL-based spherical nanoparticles within peritoneal tumor implants after intraperitoneal as opposed to intravenous (IV) administration[39]. Previous investigations have also reported that PEO-*b*-PCL-based worm-like micelles (as opposed to nanospheres) may achieve enhanced penetration through dense tumor tissues[40, 41].

Here, we sought to explore the size and shape dependence of PEO-*b*-PCL-based nanoparticles to accumulate in pancreatic tumors in hopes of identifying key physical characteristics that may enhance drug delivery. While other studies have explored the size dependencies of nanoparticles to accumulate in pancreatic tumor xenografts[28], the *Kras*- and *p53*-mutant genetically-engineered mouse model (*KPC*; see *Materials and Methods*) more readily recapitulates the key genetic, histologic, and microenviromental features of PDAC[33, 34, 42, 43] (Figure 1A, 1B and Supplementary Figure S1). Previous work revealed that transplant and autochthonous PDAC models display marked differences in drug delivery. Specifically, transplant tumors show greater responses to chemotherapy and

increased perfusion compared to the autochthonous PDAC model. Further, both human and mouse transplanted tumors exhibit greater vascularity (*i.e.,* greater blood vessel numbers and smaller vessel-to-tumor cell distances) than their naturally arising counterparts.[8] As such, we sought to conduct a comparative study of nanoparticle delivery between the autochthonous *KPC* and traditional transplant models.

We first focused on identifying fabrication conditions that could give rise to nanoparticles that differed with respect to size and shape, utilizing two PEO-*b*-PCL compositions (PEO_{5k}-PCL_{10k} and PEO_{5k}-PCL_{16k}), a homopolymer of PCL_{30k}, and two lipophilic encapsulants that could be loaded within the resultant nanoparticles (Figure 1C). The near-infrared (NIR-) emissive carbocyanine dye DiR (1,1′-dioctadecyl-3,3,3′,3′-tetramethylindotricarbocyanine iodide) was selected as a model imaging agent and a novel lipophilic prodrug of oxaliplatin (C_{16}-oxaliplatin(IV)-C_{16}) was synthesized for nanoparticle-based encapsulation and delivery to pancreatic tumors. Encapsulation of lipophilic DiR in PEO-*b*-PCL-based nanoparticles has previously been used to enable their accurate *in vivo* imaging in subcutaneous tumor xenograft models.[44, 45] We have also utilized DiR that was encapsulated in PEO-*b*-PCL-wrapped lanthanide nanoparticles to successfully image and compare the extent of tumor localization after either intraperitoneal or intravenous administration into a disseminated cell-line xenograft model of ovarian cancer, validating tumor cell (delineated by emission of red fluorescent protein, RFP) and nanoparticle biodistribution (demarcated by the non-overlapping NIR emission of DiR) *in vivo* as well as *ex vivo* both in whole-excised organs and in tissue sections via microscopy.[39]

To generate nanoparticles of varying size and shape for comparative analyses, we dissolved the PEO-*b*-PCL copolymers with and without the PCL homopolymer and/or the lipophilic encapsulants (*i.e.*, DiR and/or C_{16}-oxaliplatin(IV)-C_{16}) into two different organic solvents (Figure 1D, Supplementary Scheme S1 and *Materials and Methods*). When dissolved in THF (and subsequently diluted into larger aqueous volumes), PEO-*b*-PCL diblock copolymers produced suspensions of spherical nanoparticles; polymers of higher molecular weight formed nanoparticles of larger size as assessed by cryogenic transmission electron microscopy (cryo-TEM; Figure 2A). Interestingly, by first dissolving in water-miscible DMF (followed by aqueous dilution), the same PEO-*b*-PCL compositions led to the formation of small worm-like micelles. To our knowledge, this is the first example by which different shaped nanoparticles are produced from the same diblock copolymer compositions simply by changing the miscible organic solvent used for aqueous emulsion. Dynamic Light Scattering (DLS) revealed that the spherical nanoparticles made from PEO_{5k}-PCL_{10k}, PEO_{5k}-PCL_{16k}, and PEO_{5k}-PCL_{16k}:PCL_{30k} (1:1 molar ratio) possessed hydrodynamic diameters of ~70 nm, ~100 nm, and ~300 nm, respectively. In contrast, worm-like micelles made from PEO_{5k}-PCL_{10k} had a mean length of 100 nm. We confirmed the stability of each PEO-*b*-PCL-based formulation; sizes (Figure 2B), polydispersity indexes (PDIs) (Figure 2C), and zeta potential measurements (Figure 2D) from all nanoparticle suspensions were relatively constant over the course of one week. Their surface charges were mildly negative and were likely attributable to their neutrally-charged PEO shells. Through the selection of different initial molecular weight compositions and the simple exchange of organic solvents used for aqueous emulsion, we were, thus, able to reproducibly generate stable polymeric nanoparticles of varying size and shape for further *in vitro* and *in vivo* experimentation.

Prior to their use for *in vivo* delivery of anticancer agents, we first examined the *in vitro* cytotoxicity of the various PEO-*b*-PCL-based nanoparticle formulations. We treated *Kras*-mutant B22 murine PDAC cells (see *Materials and Methods*) with different concentrations of PEO-*b*-PCL-based nanoparticles of varying size and morphology and measured *in vitro* cell viability at 72 h (Supplementary Figure S2). The IC_{50} values were determined to be 10, 17.8 and 177.8 mg/mL (corresponding to 0.5, 0.7, and 11.9 mM of polymer) for PEO_{5k}-PCL_{16k} (THF), PEO_{5k}-PCL_{16k}/PCL_{30k} (THF), and PEO_{5k}-PCL_{10k} (DMF) nanoparticles, respectively. The cytotoxicity of each nanoparticle formulation correlated with its decreasing size and spherical shape: the toxicity imparted by PEO_{5k}-PCL_{16k} (THF; 100 nm diameter spherical micelles) > PEO_{5k}-PCL_{16k}/PCL_{30k} (THF; 300 nm-diameter spherical micelles) > PEO_{5k}-PCL_{10k} (DMF; 100 nm-length worm-like micelles). The worm-like micelles displayed the lowest toxicity on B22 cells as compared to each spherical nanocarrier. While smaller particles may have been expected to introduce slightly more cytotoxicity (at a given polymer concentration) due to improvements in intracellular uptake, the dramatic differences in cytotoxicity between nanoparticles of different shape but of the same overall dimensions was not expected and warrants further study. Nevertheless, these data confirmed that the PEO-*b*-PCL-based nanoparticles were suitably non-toxic for *in vivo* use.

To facilitate *in vivo* optical imaging of PEO-*b*-PCL-based nanoparticles, we loaded them with the NIR fluorophore DiR (see *Materials and Methods*). We observed linear concentration-dependent changes in the fluorescence emission (Figure 3A) and the solution absorption of DiR (Figure 3B and Supplementary Figure S3) when encapsulated in PEO_{5k}-PCL_{16k}–based nanospheres in water. With increasing DiR concentrations, emission and absorbance initially rose but then declined (Figure 3A and 3B), likely due to the self-quenching effect and solubility limit, respectively, of DiR confined in the polymer shell. Consistent with the lowered energy states imparted by the self-quenching and stacking of dye molecules, the peak emission wavelength of DiR displayed a bathochromic shift with increasing concentration in nanoparticle suspensions. To minimize self-quenching, we adopted an initial solution concentration of DiR equal to 5 μM for generation of all nanoparticles used for subsequent *in vivo* studies. To ensure that this loading concentration enabled linear concentration-dependent detection of particles by *in vivo* imaging, we next administered DiR-encapsulated PEO_{5k}-PCL_{16k}–based nanospheres at different concentrations to nude mice by IV tail-vein injection. We subsequently measured the fluorescence intensities values of the particles in blood. We observed an increasing linear correlation between fluorescence efficiency and the DiR concentration at the administered dose level (Figure 3C). We also measured the effects of DiR loading on the chemical properties of all the various nanoparticle formulations. While their final concentrations of encapsulated DiR varied by as much as 2-fold in different solutions (Table 1), the DiR-loaded nanoparticles were highly photostable in water, in phosphate-buffered saline (PBS), and in fetal-bovine serum (FBS) (Figure 3D).

Delivery of PEO-*b*-PCL-based nanoparticles to allografted PDAC tumors in mice

We evaluated whether the efficiency of tumor accumulation of our PEO-*b*-PCL-based nanoparticles depended on their size and/or shape, using an allografted murine model of PDAC. We transduced B22 *Kras; p53* mutant murine PDAC cells derived from a mouse model that closely recapitulates the human disease[46] with a retroviral construct, permitting expression of both luciferase (LUC; for *in vivo* imaging) and green fluorescence protein (GFP; for immunofluorescence analysis of tumor sections). We transplanted these cells into the flanks of immunocompromised nude mice, allowing for subcutaneous tumor growth, and then administered various DiR-encapsulated, PEO-*b*-PCL-based nanoparticle formulations via IV tail-vein injection. The nanoparticles were monitored by their DiR fluorescence intensities (λ_{ex}= 710 nm; λ_{em}= 800 nm) in tumors/organs (for biodistribution studies) and in blood (for pharmacokinetic analysis) by IVIS imaging at various time points. For the spherical nanoparticles, circulation half-lives decreased as a function of increasing particle size (Table 1 and Supplementary Figures S4–S6), which was consistent with previously reported studies[47]. The worm-like micelles (100 nm in length) had a $t_{1/2}$ = (6.6 ± 1.9) h (Figure 4A and Supplementary Figure S7), which was significantly shorter than the $t_{1/2}$ of the 100 nm-diameter spherical nanoparticles (10.9 ± 1.0 h; Table 1). Fluorescence imaging (of nanoparticles) was spatially mapped to luminescence signals (from the tumors; *e.g.,* as depicted for the 100 nm-length worm-like micelles in Figure 4A) to determine the extent of nanoparticle accumulation within tumors as compared to other organs. Note that 80–90% of the maximal tumor accumulation for each nanoparticle formulation was achieved by 24 h after intravenous administration (Supplementary Figure S4–S7).

The 300-nm diameter spherical nanoparticles displayed minimal accumulation in subcutaneous (SQ) tumors as compared to their 100 nm- or 70 nm-diameter spherical counterparts or to the 100 nm-length worm-like micelles (Supplementary Figure S4–S7); in particular, the later construct showed improved tumor accumulation (Table 1), supporting its further development as a pancreatic drug delivery platform. At 72 h post-injection, mice were sacrificed and their major organs were dissected to measure DiR fluorescence distribution *ex vivo (e.g.,* Figure 4A, right insert). The fluorescence radiant efficiency of every organ was normalized to that of the liver in the same mouse (Figure 4B). For all injected suspensions (except for the 300 nm-diameter nanospheres), the tumors showed the highest accumulation of PEO-*b*-PCL-based nanoparticles as compared to all other organs (n=5 mice per formulation).

There were no significant differences in the relative tissue distributions of 70 nm- and 100 nm-diameter spherical nanoparticles as compared to the 100 nm-length worm-like micelles, revealing similar *ex vivo* tumor distribution profiles for the injected doses. In contrast, the relative accumulation of the 300 nm spherical nanoparticles was lower in the tumors than in the liver and was highest in the spleen, consistent with its clearance by the mononuclear phagocytic system (MPS)[47]. Together, these data suggest that 100 nm-diameter nanoparticles may be delivered efficiently to allograft PDAC tumors *in vivo*. While exhibiting similar relative *ex vivo* biodistribution profiles (at 24 h after injection), the worm-

like micelles demonstrated a shorter overall circulation half-life and an enhanced *in vivo* tumor accumulation as compared to the spherical nanoparticles (Table 1), which possessed comparable overall sizes and which were constructed from the same PEO-*b*-PCL composition, highlighting the potential for shape alterations to improve nanoparticle delivery.

Delivery of PEO-*b*-PCL-based nanoparticles to autochthonous PDAC tumors in mice

Previous work has suggested significant differences in vascularity, blood flow, and chemotherapeutic drug delivery between transplanted and autochthonous models of PDAC[8]. In particular, autochthonous mouse models that harbor mutations in the proto-oncogene *Kras* and the tumor suppressor gene *p53* generate pancreatic tumors with a dense desmoplastic stroma[33, 34, 43]; they demonstrate the hallmark genetic and histologic features observed in human tumors[42]; and, they exhibit hypoperfusion and reduced drug delivery as compared to allograft models[8]. As discussed previously (*vide supra*), the potential for vascularity to affect nanoparticle delivery to pancreatic tumor cells has been explored using xenograft models of human cell lines that induce extensive stroma, suggesting a strong dependence on nanoparticle size. No prior work has examined the effects of size on nanoparticle accumulation in autochthonous *Kras;p53* mutant tumors or those of nanoparticle shape on ultimate drug delivery to hypoperfused pancreatic tumors.

We generated *Kras;p53* mutant tumors, using a genetically-engineered immunocompetent mouse model of PDAC,[8, 32, 33] and administered our PEO-*b*-PCL-based nanoparticles (of varying size and shape) via IV tail-vein injection. Whole-animal fluorescence imaging by IVIS was used to independently monitor tumor growth (by tomato red fluorescent protein - RFP; see *Materials and Methods*) and nanoparticle location (by DiR; Figure 4C). 24 h after nanoparticle injection, mice were sacrificed and their organs were harvested to measure the relative *ex vivo* fluorescence distribution of the tumor cells and the nanoparticles. The harvested pancreas revealed strong RFP (Figure 4D) and DiR signals (Figure 4E), verifying successful delivery of the polymeric nanoparticles to the primary pancreatic tumor(s) in the autochthonous model. Note that normalization of emission intensities where conducted with respect to the organ that displayed the largest value in each data set, which was the pancreas in the case of RFP emission (*i.e.,* the organ of highest PDAC cell localization) and the liver in the case of DiR emission (*i.e.*, the healthy organ of greatest NP accumulation). A high RFP signal was also detected in the dissected intestines and stomach, likely due to the local spread of primary tumor cells. While the 100-nm diameter nanospheres appeared to demonstrate higher tumor accumulation than the more modest accrual levels displayed by the 300-nm diameter nanospheres, the results obtained with either formulation were not significantly different when compared to the relative tumor accumulation levels for the 70 nm-diameter nanospheres and the 100 nm-length worm-like micelles. These data, thus, reveal that nanoparticles as large as 100 nm are capable of readily accumulating in the poorly-permeable pancreatic tumor(s) of the autochthonous model. Moreover, we did not observe a significant advantage of the worm-like micelle shape in improving delivery to

these primary pancreatic tumors, differing from reported studies claiming their improved capabilities for solid tumor penetration[41].

To more carefully assess nanoparticle delivery at the cellular level, we analyzed the spatial distribution of DiR fluorescence (which identified nanoparticle locations; white) relative to the tumor cells (seen by RFP imaging; red) in frozen sections of tumors that were excised from treated mice and fixed at 24 h after nanoparticle administration (Figure 4F and Supplementary Figure S8). There were no significant differences between the four nanoparticle formulations with respect to the mean distances between nanoparticles and their nearest tumor cells (Figure 4G). While the overall percentage of the delivered dose was lower, even the 300 nm-diameter nanospheres displayed comparable nanoparticle-to-tumor distances as compared to the smaller-sized particles. While the possibility exists that differences in tumor accumulation might be observed at longer or shorter time points after the administration of different nanoparticle formulations, the results would support that once nanoparticles extravasate within pancreatic tumors, their ultimate penetration distance is independent of their size or shape.

Generation of oxaliplatin-loaded nanoparticles

We next evaluated the capacity of our nanoparticles to deliver a chemotherapeutic agent to pancreatic tumors. As a proof-of-principle example, we chose oxaliplatin, which is a platinum-containing anticancer agent used in first-line therapy of human PDAC[3]. To generate an oxaliplatin-loaded nanoparticle, we constructed a novel lipophilic oxaliplatin(IV) prodrug (C_{16}-oxaliplatin(IV)-C_{16}), where oxaliplatin was oxidized and conjugated to palmitic acid (Figure 1C). The lipophilic prodrug was subsequently encapsulated in the hydrophobic core of PEO-*b*-PCL-based nanoparticles during their fabrication (Figure 1D and Supplementary Scheme S1). By measuring the relative fluorescence yield and platinum (Pt) content of the final nanoparticle suspensions, we determined that the optimal polymer-to-oxaliplatin (P:O) weight ratio for formation was 100:10, suggesting that 10 wt% loading of nanoparticles with the lipophilic oxaliplatin(IV) prodrug was the most efficient level for incorporation (Figure 5A). DLS measurements revealed that nanoparticles formed at a P:O=100:10 remained ~100 nm in dimension (Figure 5B), which was similar to the results obtained with their unloaded PEO_{5k}-PCL_{16k}-based counterparts. Cryo-TEM images showed that the DiR-containing PEO-*b*-PCL-based nanoparticles retained a worm-like architecture after oxaliplatin(IV) loading (Figure 5C). Thus, it was determined that the oxaliplatin species could be readily incorporated within the micelles without altering nanoparticle size or shape.

We next investigated the drug release profiles of the oxaliplatin(IV)-loaded worm-like micelles. PEO-*b*-PCL-based nanoparticles are known to be stable at neutral pH, while acidic conditions, such as those found within endosomes, facilitate release of their contents[36, 38]. Under neutral or acidic pH conditions and in the presence of low concentrations of exogenously added glutathione (GSH), platinum (Pt) release remained minimal; at an acidic pH and with higher GSH concentrations, which mimicked conditions known to exist within tumor cells [48], increasing concentrations of free Pt species were detected in nanoparticle suspensions over time (Figure 5D). Pt release from worm-like micelles was, thus, found to

be triggered under acidic and reductive *in situ* conditions, supporting that similar release features could be expected after the rapid uptake of the worm-like micelles within *in vivo* tumor locations. It should be noted that the shortened circulatory half-life of oxaliplatin(IV)-loaded worm-like micelles would be expected to reduce premature drug release prior to systemic nanoparticle clearance. Given these desirable features, we next examined the *in vitro* potency of the drug-laden micelles as compared to free oxaliplatin in both murine (B22) and human (8988T) PDAC cell lines (Supplementary Figure S9). From their IC_{50} values, it was evident that free oxaliplatin and oxaliplatin(IV)-loaded worm-like micelles exhibited similar *in vitro* antitumor activity; note that cellular incubation with unloaded PEO-*b*-PCL-based nanoparticles of varying size and shape did not result in comparable cellular toxicity, supporting the biocompatibility of the nanoparticle carrier. Empty nanoparticles that were incubated with B22 and 8999T cells at concentrations that were equivalent to the *in vivo* dose used for IV tail-vein injection (*i.e.,* NP1: 5.2 mM or 78 ug/uL of PEO-*b*-PCL copolymer) did not result in significant *in vitro* cytotoxicity (Supplementary Figures S9D and S9H, respectively).

In vivo delivery and tumor retention of oxaliplatin(IV)-loaded PEO-*b*-PCL-based micelles

Following administration to nude mice harboring B22 subcutaneous pancreatic tumors, we compared the delivery and retention of our oxaliplatin(IV)-loaded worm-like micelles with equivalent doses of the free drug formulation of unmodified oxaliplatin. Pharmacokinetic analyses of the Pt content of blood samples taken at various time points after IV tail-vein injection of free oxaliplatin revealed its short circulatory half-life ($t_{1/2}$ = 1.88 h; Supplementary Figure S10A). The circulatory half-life of oxaliplatin was increased by over three-fold (to 6.5 ± 0.7 h) when loaded within and delivered by DiR-containing worm-like micelles (as measured by DiR fluorescence; Supplementary Figure S10B). Note that the half-life of the drug-laden worm-like micelles was similar to that of their unloaded counterparts ($t_{1/2}$ = 6.6 ± 1.9 h), suggesting that loading of the Pt species does not slow nor accelerate the circulation time of the nanoparticles in blood.

We further examined whether the worm-like micelles could enhance drug delivery to poorly vascularized tumors, using the autochthonous KPC model of PDAC. The Pt content of various organs was determined after IV tail-vein injection of either oxaliplatin(IV)-loaded worm-like micelles (NP-oxaliplatin) or free oxaliplatin. NP-oxaliplatin displayed both a relative (with respect to other organs) and an absolute increase (~7-fold higher amounts) in the levels of Pt accumulation within the pancreas as compared to the free drug formulation at 24 h and as assessed by atomic absorption spectroscopy (AAS) (Figure 5E). Note that the pancreas is the major organ wherein the tumors are located in these mice; hence, it serves as a surrogate to evaluate the extent of intratumoral accumulation. We also measured the amounts of Pt that persisted within the pancreatic tumors (as measured by AAS) of SQ-allografted mice that were administered either NP-oxaliplatin or free oxaliplatin at identical dose equivalents and that were then sacked at similar time intervals. Importantly, the Pt content of the tumors was prolonged after worm-like micelle delivery, exhibiting a retention half-life that was ~50× that of free oxaliplatin, which was otherwise rapidly cleared from the

tumor microenvironment ($t_{1/2}$ = 5.9 h; Figure 5F). Together, these data reveal that the 100 nm-length, PEO-*b*-PCL-based worm-like micelles are capable of delivering drugs to poorly-permeable pancreatic tumors with improved biodistribution and prolonged tumor retention as compared to free drug formulations.

As nab-paclitaxel is an established first-line therapy, and given the recent approval of an irinotecan-containing nano-liposome[17], novel nanoparticle therapeutics are garnering considerable interest in pancreatic cancer. To date, however, there have been few published studies that have sought to examine the effects of nanoparticle size on tumor penetration in murine models of PDAC. Using SQ models, Cabral et al.[28] and Wang et al.[31] have reported that nanoparticles that are sub-30 nm in diameter augment tumor uptake while those that are larger than 100 nm exhibit little to no accumulation, presumably due to size-dependent limitations to nanoparticle extravasation. In contrast to these findings and by using a similar SQ model of PDAC, Kobes et al. demonstrated significant tumor uptake for polymeric nanoparticles that were greater than 450 nm in size[49]. Additional investigations have shown that ultra-small nanoparticles (< 10 nm in size) demonstrate improved tumor uptake in similar models[15, 50].

A few studies have been performed in more advanced model systems, including in patient-derived xenograft (PDX) and in syngeneic orthotopic transplant models of PDAC; they have demonstrated enhanced tumor uptake of inorganic nanoparticles that range in size from 40 to 125 nm[51, 52]. These findings, however, contradict those of another study that has compared the sizes of gold nanoparticles in a different syngeneic transplant model, determining that nanoparticles that are < 20 nm in size provide the best tumor accumulation outcomes[53]. In general, each of these studies has failed to account for differences in tumor neovascularization, proliferation rates, and/or the extent and impact of the tumor stroma on influencing nanoparticle accumulation and penetration in their particular model system, which further complicates the generalizability of their findings for the development of clinical nanoparticle formulations for human PDAC.

To better characterize the requisite physical properties for future therapeutic applications, we performed a systematic study to evaluate the effects of size and shape on the ability of nanoparticles to deliver an anticancer agent in two different murine models of PDAC. We found major influences imparted by the size and shape of nanoparticles on their blood circulation half-lives, on the extent of the administered dose that dynamically accumulates within the tumors, and on the durations of *in vivo* tumor retention. These results would indicate that nanoparticle size and shape does affect vascular circulation through physical interactions that mediate biological phenomena (*e.g.*, opsonization of proteins that promote plasma clearance and/or traversing of gap junctions between compromised endothelial cells that enable tumor extravasation[54]). In contrast to the aforementioned claims that nanoparticles that are larger than 30 nm in diameter are unable to accumulate in ectopically or orthoptically transplanted PDAC models,[28, 31, 55] our current study supports that particles that are significantly larger (*e.g.*, 100 or even 300 nm in diameter) may preferentially extravasate into the perivascular spaces of pancreatic tumors.

We also observed some modest differences in nanoparticle behavior in the two different murine models of PDAC; the worm-like micelles may accumulate somewhat better in the transplanted model whereas the spherical nanoparticles seemed to demonstrate an improved tumor accretion in the autochthonous model. The autochthonous model is considered to more closely mimic the human disease, particularly in terms of the presence of a dense tumor stroma. While it is possible that spherical nanoparticles are able to better amass in these tumors, it is notable that no discernable dependencies between nanoparticle sizes and their ultimate diffusion distances to the nearest tumor cell clusters were observed; particles as large as 300 nm in diameter were still able to achieve mean nanoparticle-to-tumor distances of ~20 μm. Reductions in nanoparticle size or changes in shape did not aid in tumor penetration, establishing this distance as perhaps the maximal diffusion limit in the autochthonous model. In contrast to the findings reported in previous studies, which have relied on less representative model systems, our data, which was obtained with the most faithful murine model available to date, suggest that ineffective drug perfusion through the desmoplastic stroma rather than biophysical limitations to nanoparticle extravasation, which may be mediated by size/shape constraints and/or poor tumor vascularity, are the major hurdles to effective PDAC therapy. Further improvements in tumor delivery and drug penetration will likely require the development of nanoparticles that address stromal and tumor cells components simultaneously. These results highlight the importance of considering the model system when testing candidate therapeutic formulations, particularly in pancreatic cancer where the tumor stroma is thought to play such a dominant role in drug penetration, susceptibility, and disease progression.

MATERIALS AND METHODS

Chemicals and Reagents

Methoxy-terminated poly(ethylene oxide)-*block*-poly(ε-caprolactone) (PEO-*b*-PCL) and methoxy-terminated poly(ε-caprolactone) (PCL) of different molecular weights were purchased from Polymer Source, Inc. (Montreal, Canada). DiR (1,1′-dioctadecyl-3,3,3′,3′-tetramethylindotricarbocyanine iodide) was purchased from Life Technologies, Inc. (Carlsbad, CA). D-luciferin potassium salt (substrate for luciferase bioluminescence) was obtained from PerkinElmer (Waltham, MA). Other chemicals, including organic solvents, i.e., tetrahydrofuran (THF) and dimethylformamide (DMF), were purchased from Sigma-Aldrich (St. Louis, MO).

Synthesis of polymeric nanoparticles

To prepare spherical DiR-loaded polymeric nanoparticles, PEO-*b*-PCL compositions of different molecular weights (*i.e.*, PEO_{5k}-PCL_{10k} and PEO_{5k}-PCL_{16k}) were individually dissolved in THF (200 μL of a 2 mM solution), mixed with DiR (10 μL of 1 mg/mL solution in THF), and added dropwise into dH_2O (4 mL); these additions were simultaneously accompanied with sonication (~ 24 watts) for 2 min at a 30% power amplitude (Q500 sonicator; Newtown, CT). Larger-sized PEO-*b*-PCL/PCL-based spherical nanoparticles were generated by mixing PEO_{5k}-PCL_{16k} (100 μL of a 2 mM solution) and PCL_{30k} (100 μL of a separate 2 mM solution) with DiR (10 μL of 1 mg/mL solution) in THF prior to aqueous dispersion. Worm-like micelles were prepared by dissolving PEO_{5k}-PCL_{10k} (200 μL of a 2

mM solution) and by mixing with DiR (10 μL of a 1 mg/mL solution) in DMF prior to addition to a larger aqueous volume.

A lipophilic oxaliplatin(IV) prodrug (C_{16}-oxaliplatin(IV)-C_{16}) was synthesized, following previously reported methods [56]; in brief, OxaPt(IV)-COOH was first generated as previously described [48] and 0.431 g were dissolved in dry DMF in a flask under stirring. Thereafter, hexadecyl isocyanate (0.263 g) was added to the solution and allowed to react at room temperature and in the dark for 24 h. The reaction product was then condensed by vacuum evaporation, precipitated in cold ethyl ether, and washed with cold ethyl ether (×2) prior to drying under vacuum. The final white powder comprised of C_{16}-oxaliplatin(IV)-C_{16} was loaded into worm-like micelles by first dissolving it in DMF (40 μL of a 22.5 mg/mL solution; *i.e.*, 0.9 mg), by subsequently adding it to a mixture of PEO_{5k}-PCL_{10k} (150 μL of a 4 mM solution; *i.e.*, 9 mg) and DiR (10 μL of a 1 mg/mL solution) in DMF, and finally by dispersing in a larger aqueous solution.

For all nanoparticle suspensions, THF or DMF was removed after polymeric nanoparticle formation by employing 3 cycles of centrifugation filtration (Amicon centrifugal unit, EMD Millipore, Billerica, MA; MWCO = 100 kDa); the purified nanoparticles were subsequently resuspended in sterile aqueous solution (*e.g.*, dH_2O, PBS, or FBS). The final suspensions were passaged through a sterile syringe filter equipped with an immobilized cellulose acetate membrane (0.45 μm; VWR International; Radnor, PA) prior to *in vitro* or *in vivo* experiments. Endotoxin assays were performed to verify the low or zero existence of endotoxin in the final suspensions, using a Pierce™ LAL Chromogenic Endotoxin Quantitation Kit (Thermo Fisher Scientific; Waltham, MA).

Compositional Analysis of Drug- and/or Dye-Loaded Nanoparticles

Different concentrations of DiR ([DiR]) in THF were measured using UV-vis spectrophotometry (DU800; Beckman Coulter UV-Vis spectrophotometer), where the peak absorbance at 755 nm was plotted versus [DiR] to obtain its extinction coefficient in THF. Aqueous suspensions of drug- and/or DiR-loaded nanoparticles were characterized, using UV-vis spectrophotometry and by fluorescence spectroscopy (FluoroMax spectrofluorometer; Horiba Jobin Yvon). Corrected absorbance values for DiR were calculated through baseline subtraction of nanoparticle light scattering, which was recorded using analogous nanoparticle formulations that did not contain DiR, and by following previously described methodologies[57–60]. The corrected absorbance values were converted to [DiR] in the aqueous suspensions by using the extinction coefficients obtained from previous DiR solutions in THF as an estimation; these measurements were conducted to determine the residual amounts of DiR in the nanoparticle solutions. The suspensions of nanoparticles (containing PEO-*b*-PCL polymer and DiR) were lyophilized and the weights of the resulting pellets, which contained the residual polymer in the formed particles or micelles (plus the weight of surviving drugs, if applicable), were recorded to obtain the final yields of the nanoparticles in the original suspensions. Note that the residual weights of the DIR dye molecules were negligible. In drug-/dye-loaded nanoparticles, samples were further analyzed using atomic absorption spectroscopy (AAS; AAnalyst 600 GFAAS instrument; PerkinElmer) to quantify the Pt content in the final nanoparticle suspensions.

In Situ Nanoparticle Characterization

Size and zeta potential measurements of nanoparticle suspensions were conducted using a Malvern Nano-ZS90 Zetasizer (Malvern Instruments, Worcestershire, UK). Particle sizes and morphologies were further visualized by cryo-TEM (JEOL 2100F Transmission Electron Microscope; Peabody, MA). Pt release was measured by adding nanoparticles containing C_{16}-oxaliplatin(IV)-C_{16} into phosphate buffers at different pH values with and without the presence of glutathione (GSH), which is a reducing agent that facilitates conversion and release of the active oxaliplatin(II) species from the nanoparticles[48]. Sample aliquots were withdrawn at different time points (n=3 replicates per time point) and were centrifuged, using a 100 kDa cut-off filtration membrane. The filtrates containing the released Pt species were collected and measured by AAS for quantification.

Cell Lines, Culture Conditions, and Viability Studies

B22 mouse PDAC cells were derived from the primary pancreatic tumors of *LSL-Kras^{G12D}; p53$^{flox/flox}$; Pdx1-CreER* mice treated with tamoxifen (Sigma) to induce oncogenic *Kras^{G12D}* activation and biallelic *p53* inactivation in the pancreas[46]. 8988T human PDAC cells were obtained from the Broad Institute Cancer Cell Line Encyclopedia, originally sourced from DSMZ-Germany. All cell lines tested negative for mycoplasma by PCR. The cells were cultured in Dulbecco's modified Eagle's medium (DMEM) supplemented with 10% fetal bovine serum (FBS) and 1% Penicillin-Streptomycin (10,000 units/mL; Life Technologies, Grand Island, NY). For viability studies, cells were plated in 96-well microplates (PerkinElmer, Waltham, MA) at a density of 5,000 cells/well and allowed to adhere overnight. Suspensions of different nanoparticles (in 1:9 v/v PBS:media) were then added to the media to different final concentrations in separate wells (n = 6 technical replicates per condition). PBS (at 1:9 v/v media) was used as a negative control. After 24, 48 or 72 h of incubation, cells were washed with fresh media (×3) and with PBS solution (×3) to remove excess particles. Cell viability was measured, using the MTT colorimetric assay or the CellTiterGlo bioluminescence assay (Promega Corporation; Madison, WI) and by following the manufactures' protocols. Normalized cell viability was calculated by dividing the net absorbance values or luminescence counts for treated cells by those obtained with the control.

Animal Studies

All animal studies were conducted under an approved protocol by the MIT Committee on Animal Care (#0714-076-17). B22 murine pancreatic cancer cells expressing luciferase (LUC) and green fluorescent protein (GFP) were generated by retroviral transduction with *LUC-IRES-GFP*. LUC and GFP expression were detected *in vitro* by using a microplate reader (Infinite 200 PRO; Tecan group Ltd., Switzerland) and *in vivo* by employing an IVIS Spectrum bioluminescent and fluorescence imaging system (PerkinElmer; Akron, Ohio). To establish a SQ tumor-xenograft model of murine PDAC, LUC^+/GFP^+ B22 cells (2 million cells) were implanted into each flank of female athymic nude mice (NCRNU-F, Taconic Biosciences; Hudson, NY) by SQ injection. To establish the autochthonous model, *Pdx1-Cre* (Stock #014647) and *p53$^{flox/flox}$* (Stock #008462) mice were obtained from the Jackson Laboratory and crossed with *LSL-Kras^{G12D}* and LSL-*p53^{R172H}* mice that had been

previously generated in our laboratory to produce *Pdx1-Cre; LSL-Kras^{G12D}*; all animals were maintained on a mixed background. Tumor growth was monitored weekly by IVIS imaging for bioluminescence measurements. Prior to administration, all nanoparticle suspensions were filter-sterilized (0.45 μm cellulose acetate filter, VWR International; Radnor, PA). The *in vivo* biodistribution patterns of DiR-loaded nanoparticles were observed by *in vivo* fluorescence imaging, gating on the Cy7.5 channel (λ_{ex} = 710 nm; λ_{em} = 800 nm). The relative locations of the tumors were also visualized at each time point via *in vivo* imaging of their LUC signals upon injection of d-luciferin (50 mg/kg) and/or by RFP imaging (λ_{ex} = 540 nm; λ_{em} = 580 nm).

For pharmacokinetic determination, blood samples (10–15 μL) were collected periodically by retro-orbital venipuncture, using quartz microcapillary tubes (Sutter Instrument; Novato, CA). The tubes were then imaged with the IVIS instrument (λ_{ex} = 710 nm; λ_{em} = 800 nm) to measure changes in DiR radiant efficiency (photons/sec/cm^2/surface area), which corrected for differences between sample measurements and whose values were converted to fluorophore concentrations, using predetermined fluorescence standard curves. By fitting to $C=C_0*e^{-kt}$, where C stands for [DiR] measured at time = t and C_0 equals the original [DiR] in blood upon injection, the value of k was determined as the decay constant of DiR-encapsulated polymeric nanoparticles in blood; this value was used to calculate the blood circulation half-life of a given formulation (*i.e.*, $t_{1/2} = \ln(2)/k$). To measure accumulation of nanoparticles in the SQ tumor xenografts, DiR fluorescence intensities (in radians) were spatially mapped to the luminescence signal area (corresponding to the tumor locations), were normalized to their initial values (immediately after nanoparticle injection), and were plotted versus time. A quadratic polynomial function was then fitted into each data set and the vertex of the parabola was determined as (t, f), where the t coordinate corresponded to the maximal tumor accumulation/retention time of the injected nanoparticle and f represented the maximal fold increase of particles in tumors post-injection (Table 1). To measure the circulation time of free oxaliplatin, mouse blood (0.4–0.5 mL) was collected by cardiac venipuncture immediately following euthanasia by CO_2 and at different time points after the mouse had been injected with free oxaliplatin (n=4 mice per time point). AAS measurements were conducted to determine the Pt content in each blood sample.

Upon completion of the *in vivo* imaging experiments, mice were sacrificed and their organs were harvested and imaged *ex vivo,* using the same imaging parameters (*vide supra*). The average photon fluxes in radians for the different reporter signals in each excised organ were quantified by gating on a region of interest (ROI), using Living Image Software V.4.5.2, for 3 separate mice per tumor type that were similarly processed. The relative signal distribution intensities (in radians) from each organ were determined. In the case of RFP emission, the intensity value measured in each organ that was excised from an autochthonous KPC mouse was normalized to that of the pancreas of each mouse, which was the organ of highest PDAC tumor cell accumulation. In the case of DiR emission in organs obtained from either SQ or KPC mice, the intensity value measured in each organ was normalized to that of the liver of each mouse, which was the healthy organ that otherwise displayed the highest nanoparticle uptake. Tissue Pt concentrations were determined by adding H_2O_2 (1 mL) and 70% HNO_3 solution (1 mL) to each of the excised organs, heating the samples (to 70 °C) until all tissues were dissolved into a clear solution, and removing the insoluble cellular fractions by

centrifugation. AAS measurements were conducted to determine the Pt content in each organ, which was determined by dividing the measured Pt level by the initial tissue weight prior to processing (g) and normalizing the resultant value to the total injected dose of Pt; as such, the data were plotted as the percentages of the injected dose of oxaliplatin per gram (%ID/g) for each organ.

Tissue Immunostaining

Mice were euthanized by CO_2 asphyxiation. Tissues were dissected, fixed overnight with cold 4% paraformaldehyde (PFA), cryoprotected with 30% sucrose, and embedded in OCT (Tissue-Tek). For tissue section analyses, 5 to 30 μm sections were cut using a Leica cryostat, air dried for 30–60 min, washed with PBS (×3), stained with DAPI (Life Technologies) for 5 min, and mounted in Vectashield (Vector Labs) prior to imaging. For immunofluorescence staining, sections were blocked with 10% v/v normal donkey serum with 0.3% Triton X-100 in PBS, stained with rabbit anti-Iba-1 (Catalog #019-19741, Wako Chemicals USA; Richmond, VA) primary antibody, donkey anti-rabbit Alexa 488 or Alexa 568 secondary antibody (Life Technologies, 1:500), and DAPI prior to mounting in Vectashield. Images were obtained using an Andor camera (Oxford Instruments, Concord, MA) attached to a Nikon 80 Eclipse 80i fluorescence microscope, using 4×, 10×, and 20× objectives. Nanoparticles (DiR labeled), tumor cells (expressing either GFP or TdTomato RFP) and stromal cells (nuclei stained with DAPI) were visualized by florescence imaging in separate channels. The following filter sets were utilized, where the suffix denotes the excitation center wavelength/bandwidth (X), the mirror cut-on wavelength or center wavelength/bandwidth (LP), and the emission center wavelength/bandwidth (M): DAPI (360/40X, 400LP, 460/50M), GFP (480/30X, 505LP, 535/40M), TdTomato RFP (540/24X, 565LP, 620/60M) and/or DiR (620/60X, 660 LP, 700/75M). Merged images were generated using ImageJ software. Nanoparticle (DiR; white) to tumor cell (TdTomato RFP; red) distances in the merged image micrographs of tumor sections from autochthonous tumor-bearing mice were quantified by choosing one PDAC cell from the periphery of each slide and then determining the average distance to the five nearest nanoparticles. Five random slides were similarly chosen for each treated mouse and the mean nanoparticle-to-tumor distances were calculated.

Statistical Analysis

Data are presented as the mean ± the standard deviation (SD). A minimum of 5 mice was used for testing of each distinct nanoparticle composition per experiment unless otherwise indicated. Student's *t*-test was conducted using GraphPad software (San Diego, USA). A *p*-value of < 0.05 was considered statistically significant.

Supplementary Material

Refer to Web version on PubMed Central for supplementary material.

Acknowledgments

This work was supported by the Charles W. and Jennifer C. Johnson Clinical Investigator Fund at the Koch Institute at MIT (P.P.G.). The authors also acknowledge the generous support of Misrock Foundation (Z.T.), the Fondation

Française pour la Recherche contre le Myélome et les Gammapathies Monoclonales (A.D.), and the Kathryn Fox Samway Foundation (P.P.G.). M.D.M. was supported by an NCI Mentored Clinical Scientist Research Career Development Award (K08-CA2080016-01) and by a KL2/Catalyst Medical Research Investigator Training award (an appointed KL2 award) from the Harvard Catalyst, The Harvard Clinical and Translational Science Center (National Center for Research Resources and the National Center for Advancing Translational Sciences), a National Institutes of Health Award KL2 TR001100), and a Conquer Cancer Foundation-American Society for Clinical Oncology (CCF-ASCO) Young Investigator Award. The content is solely the responsibility of the authors and does not necessarily represent the official views of Harvard Catalyst, Harvard University and its affiliated academic healthcare centers, or the National Institutes of Health. T.J. is a Howard Hughes Medical Institute Investigator, the David H. Koch Professor of Biology, and a Daniel K. Ludwig Scholar.

References

1. Siegel RL, Miller KD, Jemal A. CA Cancer J Clin. 2017; 67(1):7–30. [PubMed: 28055103]
2. Ryan DP, Hong TS, Bardeesy N. N Engl J Med. 2014; 371(22):2140–1.
3. Conroy T, Desseigne F, Ychou M, Bouche O, Guimbaud R, Becouarn Y, Adenis A, Raoul JL, Gourgou-Bourgade S, de la Fouchardiere C, Bennouna J, Bachet JB, Khemissa-Akouz F, Pere-Verge D, Delbaldo C, Assenat E, Chauffert B, Michel P, Montoto-Grillot C, Ducreux M. Groupe Tumeurs Digestives of U, Intergroup P. N Engl J Med. 2011; 364(19):1817–25. [PubMed: 21561347]
4. Von Hoff DD, Ervin T, Arena FP, Chiorean EG, Infante J, Moore M, Seay T, Tjulandin SA, Ma WW, Saleh MN, Harris M, Reni M, Dowden S, Laheru D, Bahary N, Ramanathan RK, Tabernero J, Hidalgo M, Goldstein D, Van Cutsem E, Wei X, Iglesias J, Renschler MF. N Engl J Med. 2013; 369(18):1691–703. [PubMed: 24131140]
5. Rasheed, ZA., Matsui, W., Maitra, A. Pathology of pancreatic stroma in PDAC. In: Grippo, PJ., Munshi, HG., editors. Pancreatic Cancer and Tumor Microenvironment. Trivandrum (India): 2012.
6. Neesse A, Algul H, Tuveson DA, Gress TM. Gut. 2015; 64(9):1476–84. [PubMed: 25994217]
7. Feig C, Gopinathan A, Neesse A, Chan DS, Cook N, Tuveson DA. Clinical cancer research : an official journal of the American Association for Cancer Research. 2012; 18(16):4266–76. [PubMed: 22896693]
8. Olive KP, Jacobetz MA, Davidson CJ, Gopinathan A, McIntyre D, Honess D, Madhu B, Goldgraben MA, Caldwell ME, Allard D, Frese KK, Denicola G, Feig C, Combs C, Winter SP, Ireland-Zecchini H, Reichelt S, Howat WJ, Chang A, Dhara M, Wang L, Ruckert F, Grutzmann R, Pilarsky C, Izeradjene K, Hingorani SR, Huang P, Davies SE, Plunkett W, Egorin M, Hruban RH, Whitebread N, McGovern K, Adams J, Iacobuzio-Donahue C, Griffiths J, Tuveson DA. Science. 2009; 324(5933):1457–61. [PubMed: 19460966]
9. Provenzano PP, Cuevas C, Chang AE, Goel VK, Von Hoff DD, Hingorani SR. Cancer Cell. 2012; 21(3):418–29. [PubMed: 22439937]
10. Jacobetz MA, Chan DS, Neesse A, Bapiro TE, Cook N, Frese KK, Feig C, Nakagawa T, Caldwell ME, Zecchini HI, Lolkema MP, Jiang P, Kultti A, Thompson CB, Maneval DC, Jodrell DI, Frost GI, Shepard HM, Skepper JN, Tuveson DA. Gut. 2013; 62(1):112–20. [PubMed: 22466618]
11. Hingorani SR, Harris WP, Beck JT, Berdov BA, Wagner SA, Pshevlotsky EM, Tjulandin SA, Gladkov OA, Holcombe RF, Korn R, Raghunand N, Dychter S, Jiang P, Shepard HM, Devoe CE. Clinical cancer research : an official journal of the American Association for Cancer Research. 2016; 22(12):2848–54. [PubMed: 26813359]
12. Wong KM, Horton KJ, Coveler AL, Hingorani SR, Harris WP. Curr Oncol Rep. 2017; 19(7):47. [PubMed: 28589527]
13. Lane LA, Qian X, Smith AM, Nie S. Annual review of physical chemistry. 2015; 66:521–47.
14. Maeda H. Advanced drug delivery reviews. 2015; 91:3–6. [PubMed: 25579058]
15. Detappe A, Kunjachan S, Sancey L, Motto-Ros V, Biancur D, Drane P, Guieze R, Makrigiorgos GM, Tillement O, Langer R, Berbeco R. J Control Release. 2016; 238:103–13. [PubMed: 27423325]
16. Detappe A, Thomas E, Tibbitt MW, Kunjachan S, Zavidij O, Parnandi N, Reznichenko E, Lux F, Tillement O, Berbeco R. Nano Lett. 2017; 17(3):1733–1740. [PubMed: 28145723]

17. Wang-Gillam A, Li CP, Bodoky G, Dean A, Shan YS, Jameson G, Macarulla T, Lee KH, Cunningham D, Blanc JF, Hubner RA, Chiu CF, Schwartsmann G, Siveke JT, Braiteh F, Moyo V, Belanger B, Dhindsa N, Bayever E, Von Hoff DD, Chen LT. Group N-S. Lancet. 2016; 387(10018):545–57. [PubMed: 26615328]
18. Meng H, Zhao Y, Dong J, Xue M, Lin YS, Ji Z, Mai WX, Zhang H, Chang CH, Brinker CJ, Zink JI, Nel AE. ACS nano. 2013; 7(11):10048–65. [PubMed: 24143858]
19. Meng H, Wang M, Liu H, Liu X, Situ A, Wu B, Ji Z, Chang CH, Nel AE. ACS nano. 2015; 9(4): 3540–57. [PubMed: 25776964]
20. Liu X, Situ A, Kang Y, Villabroza KR, Liao Y, Chang CH, Donahue T, Nel AE, Meng H. ACS nano. 2016; 10(2):2702–15. [PubMed: 26835979]
21. Miyata K, Nishiyama N, Kataoka K. Chemical Society reviews. 2012; 41(7):2562–74. [PubMed: 22105545]
22. Cabral H, Nishiyama N, Kataoka K. Accounts of chemical research. 2011; 44(10):999–1008. [PubMed: 21755933]
23. Cabral H, Kataoka K. J Control Release. 2014; 190:465–76. [PubMed: 24993430]
24. Lytton-Jean AK, Kauffman KJ, Kaczmarek JC, Langer R. Cancer treatment and research. 2015; 166:293–322. [PubMed: 25895874]
25. Cheng CJ, Tietjen GT, Saucier-Sawyer JK, Saltzman WM. Nat Rev Drug Discov. 2015; 14(4):239–47. [PubMed: 25598505]
26. Movassaghian S, Merkel OM, Torchilin VP. Wiley interdisciplinary reviews. Nanomedicine and nanobiotechnology. 2015; 7(5):691–707. [PubMed: 25683687]
27. Cabral H, Murakami M, Hojo H, Terada Y, Kano MR, Chung UI, Nishiyama N, Kataoka K. Proceedings of the National Academy of Sciences of the United States of America. 2013; 110(28): 11397–402. [PubMed: 23801758]
28. Cabral H, Matsumoto Y, Mizuno K, Chen Q, Murakami M, Kimura M, Terada Y, Kano MR, Miyazono K, Uesaka M, Nishiyama N, Kataoka K. Nature nanotechnology. 2011; 6(12):815–23.
29. Mochida Y, Cabral H, Miura Y, Albertini F, Fukushima S, Osada K, Nishiyama N, Kataoka K. ACS nano. 2014; 8(7):6724–38. [PubMed: 24927216]
30. Kaida S, Cabral H, Kumagai M, Kishimura A, Terada Y, Sekino M, Aoki I, Nishiyama N, Tani T, Kataoka K. Cancer research. 2010; 70(18):7031–41. [PubMed: 20685894]
31. Wang J, Mao W, Lock LL, Tang J, Sui M, Sun W, Cui H, Xu D, Shen Y. ACS nano. 2015; 9(7): 7195–206. [PubMed: 26149286]
32. Hingorani SR, Petricoin EF, Maitra A, Rajapakse V, King C, Jacobetz MA, Ross S, Conrads TP, Veenstra TD, Hitt BA, Kawaguchi Y, Johann D, Liotta LA, Crawford HC, Putt ME, Jacks T, Wright CV, Hruban RH, Lowy AM, Tuveson DA. Cancer Cell. 2003; 4(6):437–50. [PubMed: 14706336]
33. Hingorani SR, Wang L, Multani AS, Combs C, Deramaudt TB, Hruban RH, Rustgi AK, Chang S, Tuveson DA. Cancer Cell. 2005; 7(5):469–83. [PubMed: 15894267]
34. Bardeesy N, Aguirre AJ, Chu GC, Cheng KH, Lopez LV, Hezel AF, Feng B, Brennan C, Weissleder R, Mahmood U, Hanahan D, Redston MS, Chin L, Depinho RA. Proceedings of the National Academy of Sciences of the United States of America. 2006; 103(15):5947–52. [PubMed: 16585505]
35. Grossen P, Witzigmann D, Sieber S, Huwyler J. Journal of Controlled Release. 2017; 260:46–60. [PubMed: 28536049]
36. Ghoroghchian PP, Li G, Levine DH, Davis KP, Bates FS, Hammer DA, Therien MJ. Macromolecules. 2006; 39(5):1673–1675. [PubMed: 20975926]
37. Qi W, Ghoroghchian PP, Li G, Hammer DA, Therien MJ. Nanoscale. 2013; 5(22):10908–15. [PubMed: 24056924]
38. Levine DH, Ghoroghchian PP, Freudenberg J, Zhang G, Therien MJ, Greene MI, Hammer DA, Murali R. Methods. 2008; 46(1):25–32. [PubMed: 18572025]
39. Tao Z, Dang X, Huang X, Muzumdar MD, Xu ES, Bardhan NM, Song H, Qi R, Yu Y, Li T, Wei W, Wyckoff J, Birrer MJ, Belcher AM, Ghoroghchian PP. Biomaterials. 2017; 134:202–215. [PubMed: 28482280]

40. Cai S, Vijayan K, Cheng D, Lima EM, Discher DE. Pharm Res. 2007; 24(11):2099–109. [PubMed: 17564817]
41. Loverde SM, Klein ML, Discher DE. Adv Mater. 2012; 24(28):3823–30. [PubMed: 22105885]
42. Waddell N, Pajic M, Patch AM, Chang DK, Kassahn KS, Bailey P, Johns AL, Miller D, Nones K, Quek K, Quinn MC, Robertson AJ, Fadlullah MZ, Bruxner TJ, Christ AN, Harliwong I, Idrisoglu S, Manning S, Nourse C, Nourbakhsh E, Wani S, Wilson PJ, Markham E, Cloonan N, Anderson MJ, Fink JL, Holmes O, Kazakoff SH, Leonard C, Newell F, Poudel B, Song S, Taylor D, Waddell N, Wood S, Xu Q, Wu J, Pinese M, Cowley MJ, Lee HC, Jones MD, Nagrial AM, Humphris J, Chantrill LA, Chin V, Steinmann AM, Mawson A, Humphrey ES, Colvin EK, Chou A, Scarlett CJ, Pinho AV, Giry-Laterriere M, Rooman I, Samra JS, Kench JG, Pettitt JA, Merrett ND, Toon C, Epari K, Nguyen NQ, Barbour A, Zeps N, Jamieson NB, Graham JS, Niclou SP, Bjerkvig R, Grutzmann R, Aust D, Hruban RH, Maitra A, Iacobuzio-Donahue CA, Wolfgang CL, Morgan RA, Lawlor RT, Corbo V, Bassi C, Falconi M, Zamboni G, Tortora G, Tempero MA, Gill AJ, Eshleman JR, Pilarsky C, Scarpa A, Musgrove EA, Pearson JV, Biankin AV, Grimmond SM. Australian Pancreatic Cancer Genome I. Nature. 2015; 518(7540):495–501. [PubMed: 25719666]
43. Muzumdar MD, Dorans KJ, Chung KM, Robbins R, Tammela T, Gocheva V, Li CM, Jacks T. Nat Commun. 2016; 7:12685. [PubMed: 27585860]
44. Cho H, Indig GL, Weichert J, Shin H-C, Kwon GS. Nanomedicine: Nanotechnology, Biology & Medicine. 2012; 8(2):228.
45. Christian DA, Cai S, Garbuzenko OB, Harada T, Zajac AL, Minko T, Discher DE. Molecular Pharmaceutics. 2009; 6(5):1343–1352. [PubMed: 19249859]
46. Friedlander SYG, Chu GC, Snyder EL, Girnius N, Dibelius G, Crowley D, Vasile E, DePinho RA, Jacks T. Cancer Cell. 2009; 16(5):379–389. [PubMed: 19878870]
47. Moghimi SM, Hunter AC, Murray JC. Pharmacol Rev. 2001; 53(2):283–318. [PubMed: 11356986]
48. Xiao H, Qi R, Li T, Awuah SG, Zheng Y, Wei W, Kang X, Song H, Wang Y, Yu Y, Bird MA, Jing X, Yaffe MB, Birrer MJ, Ghoroghchian PP. J Am Chem Soc. 2017; 139(8):3033–3044. [PubMed: 28166401]
49. Kobes JE, Daryaei I, Howison CM, Bontrager JG, Sirianni RW, Meuillet EJ, Pagel MD. Pancreas. 2016; 45(8):1158–66. [PubMed: 26918875]
50. Kunjachan S, Detappe A, Kumar R, Ireland T, Cameron L, Biancur DE, Motto-Ros V, Sancey L, Sridhar S, Makrigiorgos GM, Berbeco RI. Nano Lett. 2015; 15(11):7488–96. [PubMed: 26418302]
51. Kelly KA, Bardeesy N, Anbazhagan R, Gurumurthy S, Berger J, Alencar H, Depinho RA, Mahmood U, Weissleder R. PLoS Med. 2008; 5(4):e85. [PubMed: 18416599]
52. Mahajan UM, Teller S, Sendler M, Palankar R, van den Brandt C, Schwaiger T, Kuhn JP, Ribback S, Glockl G, Evert M, Weitschies W, Hosten N, Dombrowski F, Delcea M, Weiss FU, Lerch MM, Mayerle J. Gut. 2016; 65(11):1838–1849. [PubMed: 27196585]
53. Saha S, Xiong X, Chakraborty PK, Shameer K, Arvizo RR, Kudgus RA, Dwivedi SK, Hossen MN, Gillies EM, Robertson JD, Dudley JT, Urrutia RA, Postier RG, Bhattacharya R, Mukherjee P. ACS nano. 2016; 10(12):10636–10651. [PubMed: 27758098]
54. Alexis F, Pridgen E, Molnar LK, Farokhzad OC. Mol Pharm. 2008; 5(4):505–15. [PubMed: 18672949]
55. Adiseshaiah PP, Crist RM, Hook SS, McNeil SE. Nat Rev Clin Oncol. 2016; 13(12):750–765. [PubMed: 27531700]
56. Feng B, Zhou F, Lu W, Wang D, Wang T, Luo C, Wang H, Li Y, Yu H. Biomater Sci. 2017; 5(8): 1522–1525. [PubMed: 28406499]
57. Ghoroghchian PP, Frail PR, Susumu K, Blessington D, Brannan AK, Bates FS, Chance B, Hammer DA, Therien MJ. Proceedings of the National Academy of Sciences of the United States of America. 2005; 102(8):2922–7. [PubMed: 15708979]
58. Ghoroghchian PP, Frail PR, Susumu K, Park TH, Wu SP, Uyeda HT, Hammer DA, Therien MJ. J Am Chem Soc. 2005; 127(44):15388–90. [PubMed: 16262400]
59. Ghoroghchian PP, Frail PR, Li G, Zupancich JA, Bates FS, Hammer DA, Therien MJ. Chem Mater. 2007; 19(6):1309–1318. [PubMed: 19079789]

60. Ghoroghchian PP, Lin JJ, Brannan AK, Frail PR, Bates FS, Therien MJ, Hammer DA. Soft Matter. 2006; 2(11):973–980.

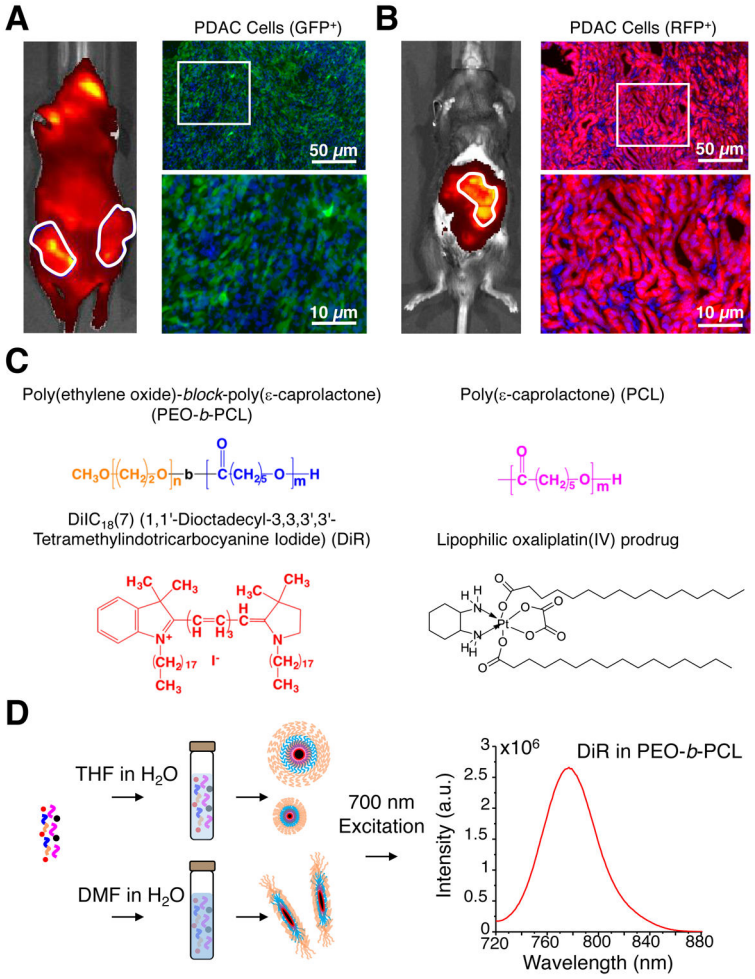

Figure 1. Fabrication of nanoparticles for delivery to transplanted and autochthonous models of PDAC

Whole animal fluorescence images and tumor micrographs illustrating differences in the microarchitecture of (A) subcutaneous green fluorescent protein (GFP)-expressing pancreatic tumor allografts, consisting of B22 *Kras;p53* mutant murine PDAC cells (green) implanted in the flanks of nude mice, and (B) autochthonous pancreatic tumors from TdTomato red fluorescence protein (RFP)-expressing primary PDAC cells (red) in *KPC* mice; desmoplastic stroma may be visualized by labeled cells (DAPI; blue) that do not have additional fluorescence protein expression in the cytoplasm. The images in the bottom right hand corner of each panel are expanded views for the purposes of high-resolution illustration. Images from additional mice of each tumor model may be found in Supplementary Figure S1 in the Supporting Information. (C) Chemical compositions utilized to form nanoparticles (PEO-*b*-PCL and PCL) and the structures of their lipophilic encapsulants (DiR and an oxaliplatin(IV) prodrug (i.e. C16-oxalipaltin(IV)-C16)). (D) Schematic illustrating differences in the fabrication conditions whereby the same chemical constituents lead to formation of different sized spherical nanoparticles or to worm-like micelles. Note that all PEO-*b*-PCL-based nanoparticle suspensions were labeled with DiR,

generating near-infrared fluorescence signals that aided in *in vitro* and *in vivo* tracking via optical imaging.

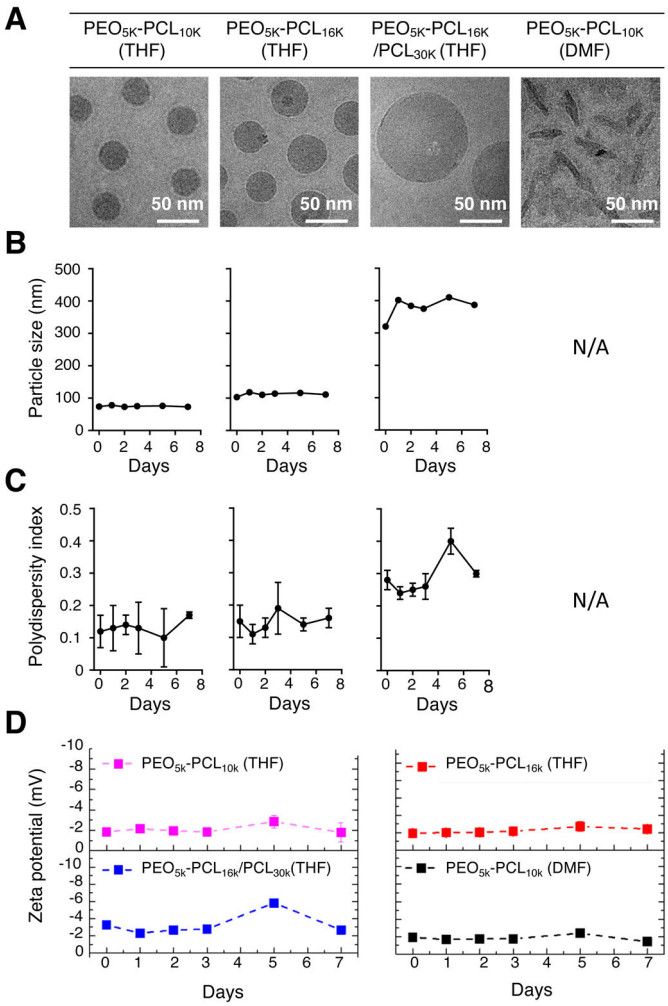

Figure 2. Characterization of PEO-*b*-PCL-based nanoparticles of varying size and shape

(A) PEO-*b*-PCL copolymers of different molecular weight were dissolved in either THF or DMF prior to aqueous emulsion. Cyro-TEM micrographs confirmed that the formation of polymer nanoparticles of varying size and shape were dependent on the selected molecular weight of the copolymer, the initial organic solvent used for dissolution, and the ultimate aqueous dispersion conditions. PEO-*b*-PCL-based nanoparticles were characterized by (B) DLS measurements, by (C) their polydispersity indices, and by (D) zeta potential measurements over a period of 7 days after formulation in aqueous suspension.

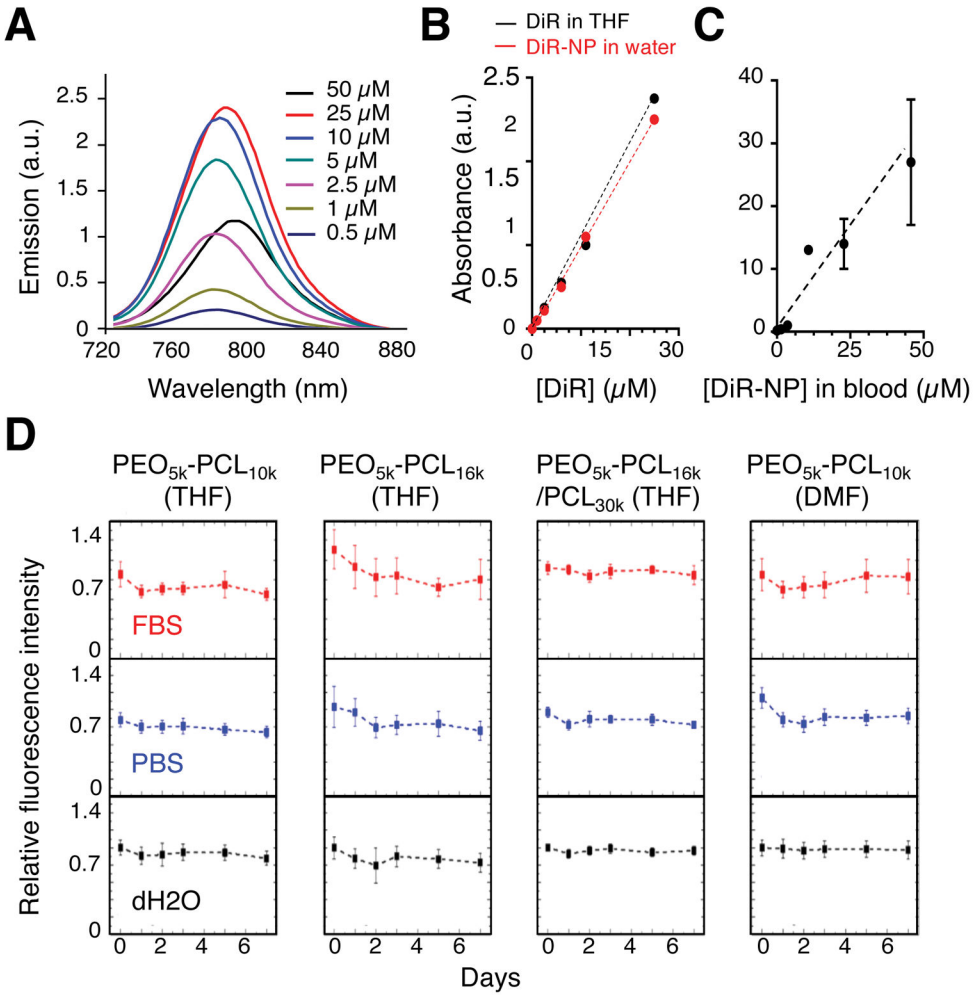

Figure 3. Properties of DiR-loaded nanoparticles

(A) Characterization of the fluorescence spectra of different concentrations of DiR encapsulated in PEO-*b*-PCL-based nanoparticles that were formed by dissolution in THF followed by aqueous dispersion; the emission spectra were recorded upon excitation at 700 nm. Similarly, the absorbance spectra of DiR were measured as a function of increasing concentration in (B) THF (DiR in THF), in PEO-*b*-PCL-based nanoparticles in aqueous suspension (DiR-NP in water), or in C) PEO-*b*-PCL-based nanoparticles in whole blood, demonstrating linear relationships. (D) The relative fluorescence intensities of each of the various DiR-loaded and PEO-*b*-PCL-based nanoparticle suspensions were examined in different solutions (fetal bovine serum – FBS; phosphate buffered saline – PBS; and dH_2O) over the course of 7 days, exhibiting stable profiles.

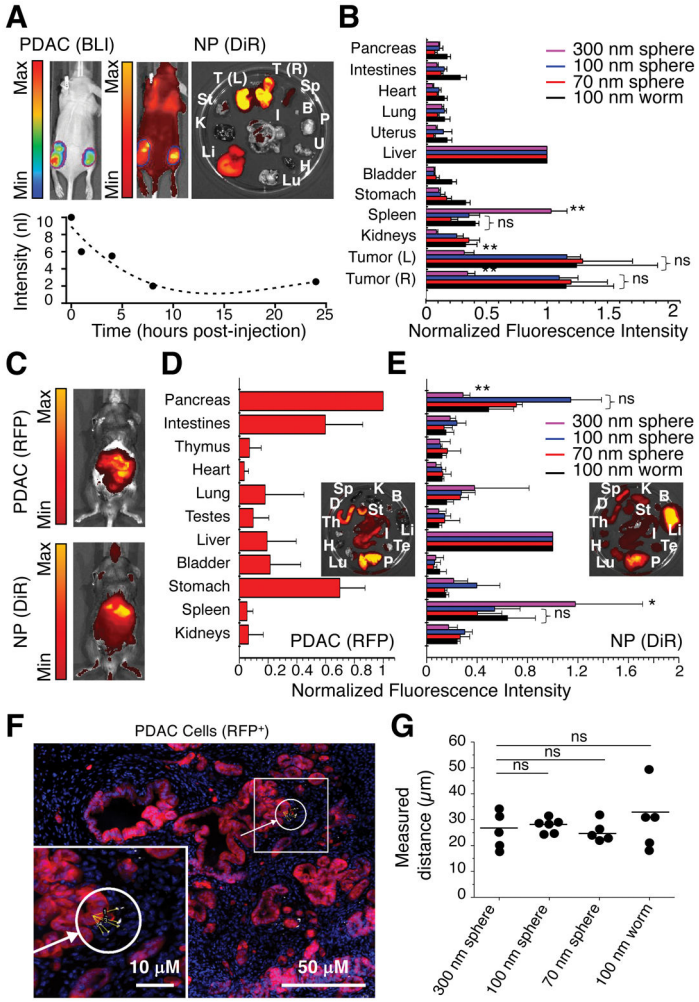

Figure 4. Comparisons of nanoparticle delivery in a SQ allograft vs autochthonous mouse model of pancreatic cancer

(A) Whole animal bioluminescence (BLI; PDAC tumor cells) and near-infrared fluorescence images (DiR; nanoparticles (NPs)) taken of the SQ mouse model of pancreatic cancer at 24 h after the administration of 100 nm-length PEO-*b*-PCL-based worm-like micelles via intravenous (IV) injection. The time course of NP clearance (as assessed by DiR fluorescence in blood samples) is found in the accompanying graph (below the *in vivo* images); note that analogous pharmacokinetic plots from additional mice that had been administered either this or an alternative NP formulation (*i.e.,* 300-, 100- or 70 nm-diameter nanospheres) may be found in Supplementary Figures S4–S7 in the Supporting Information. *Ex vivo* images of excised organs were taken at the time of animal sacrifice (*i.e.,* 24 h after NP injection) and the displayed images correspond to a mouse injected with 100 nm-length worm-like micelles (inset, right); as arranged in clockwise order, T(L): left tumor, T(R): right tumor, Sp: spleen, B: bladder, I: intestines, P: pancreas, U: uterus (plus parametria), H: heart, Lu: lung, Li: liver, K: kidneys, and St: stomach. (B) Relative *ex vivo* biodistribution profiles of various NP formulations in the SQ mouse model as determined from quantification of DiR fluorescence signals obtained from *ex vivo* images. Note that normalization of emission data was performed with respect to the healthy organ of highest

DiR emission (*i.e.,* NP accumulation), which was determined to be the liver. (C) Whole-animal images of RFP (PDAC tumor cells) and DiR (NP) fluorescence in the autochthonous *KPC* mouse model of pancreatic cancer; images were taken at 24 h after the administration of 100 nm-diameter nanospheres via IV (tail-vein) injection. (D) RFP signals (illustrating tumor cell locations) and (E) DiR signals (visualizing NP distribution) in the excised organs from a *KPC* mouse are shown as insets and adopt the same nomenclature as in (A). Note that the Th: thymus, D: duodenum, and Te: testes are further demarcated. Normalization of emission intensities where again conducted with respect to the organ that displayed the largest value in each data set, which was the pancreas in the case of RFP emission (*i.e.,* the organ of highest PDAC cell localization) and the liver in the case of DiR emission (*i.e.*, the healthy organ of greatest NP accumulation). (F) Fluorescence micrograph demonstrating the intratumoral location of 100-nm diameter nanospheres (DiR; white) with respect to PDAC cells (RFP; red) and stromal cells (DAPI; blue) in a tumor section from an autochthonous *KPC* mouse. Images from tumor sections taken from additional *KPC* mice, including ones that were administered different NP formulations (*i.e.,* 300 nm-diameter nanospheres, 70 nm-diameter nanospheres, or 100 nm-length nanoworms) may be found in Supplementary Figure S8 in the Supporting Information. (G) The ultimate nanoparticle-to-tumor distances for different NP formulations that vary with respect to size and shape as assessed in autochthonous pancreatic tumor sections from *KPC* mice. (ns: not statistically significant; **p-value < 0.001; unpaired t-test).

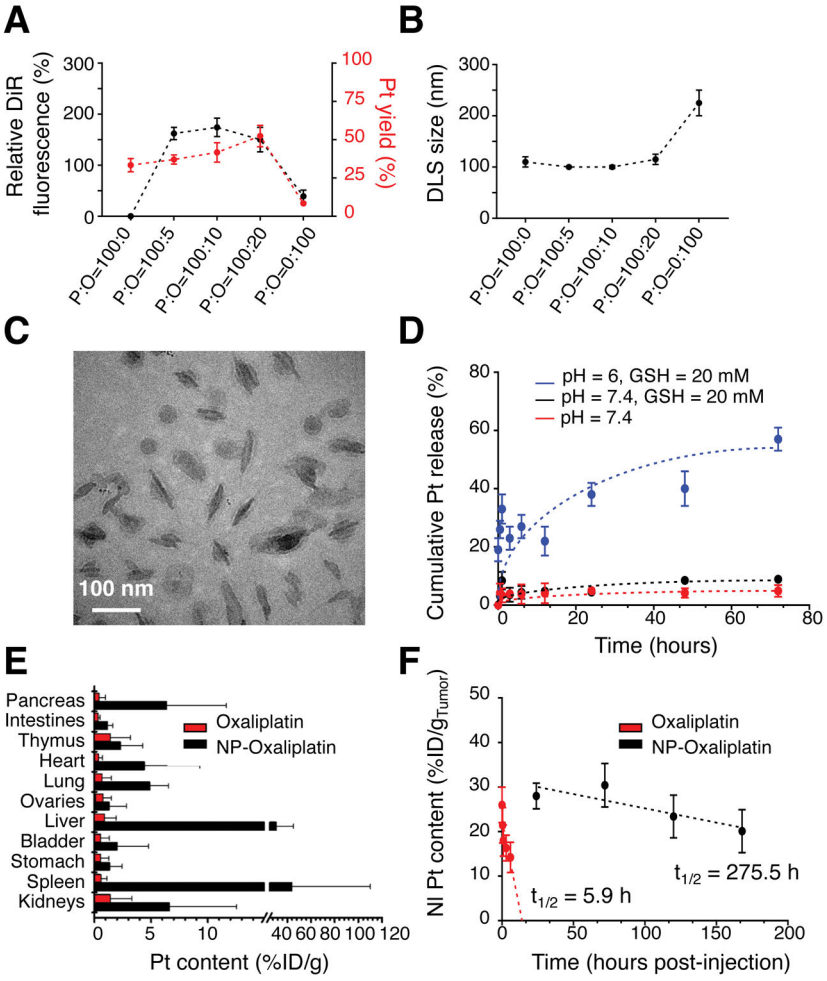

Figure 5. Characterization and delivery of oxaliplatin-loaded PEO-*b*-PCL-based worm-like micelles

(A) Relative DiR fluorescence intensities and the loading efficiencies of a lipophilic oxaliplatin(IV) prodrug (based on platinum (Pt) content) in PEO-*b*-PCL-based worm-like micelles as a function of the initial weight ratio of polymer (P) to oxaliplatin (O) used for nanoparticle incorporation (P:O ratio). (B) DLS of worm-like micelles as a function of the initial P:O ratio. (C) Cryo-TEM micrograph of worm-like micelles that are maximally loaded with the lipophilic oxaliplatin(IV) prodrug (and that were formed at an initial P:O = 100:10). (D) *In situ* release of free oxaliplatin (based on Pt) from oxaliplatin(IV)-loaded PEO-*b*-PCL-based worm-like micelles under various environmental conditions. (E) Pt content in excised organs based on the injected dose of oxaliplatin per gram tissue (%ID/g) and as assessed at 24 h after intravenous (tail-vein) injection of either free oxaliplatin or oxaliplatin(IV)-loaded PEO-*b*-PCL-based worm-like micelles in the autochthonous *KPC* model. Note that the pancreas is the major organ wherein the tumors are located in these mice; hence, it serves as a surrogate to evaluate the extent of intratumoral accumulation. (F) Differences in the *in vivo* tumor persistence of oxaliplatin after delivery by worm-like micelles vs. the free drug formulation in the SQ PDAC model.

Table 1

Comparisons of physicochemical properties and the resultant *in vivo* performance of PEO-*b*-PCL-based nanoparticles fabricated from different molecular weight polymers and by selection of the initial organic solvent used for polymer dissolution and aqueous dispersion.

	PEO_{5K}-PCL_{10K} (THF)	**PEO_{5K}-PCL_{16K} (THF)**	**PEO_{5K}-PCL_{16K}/PCL_{30K} (THF)**	**PEO_{5K}-PCL_{10K} (DMF)**
Particle shape	Sphere	Sphere	Sphere	Worm
Particle size by DLS (nm)	69.6 ± 1.1	106.2 ± 3.8	312.7 ± 10.4	111.3 ± 5.3
PDI by DLS (nm)	0.128±0.029	0.103±0.045	0.206±0.045	0.144±0.027
Zeta potential (mv)	−1.9	−1.84	−2.92	−1.74
% Yield of NP (by polymer)	58.8±7.6	59.5±8.7	55.4±3.0	55.8±1.0
% Yield of NP (by DiR fluorescence)	54.9±5.8	63.2±7.3	26.9±3.9	38.9±3.3
***In vitro* IC_{50} of Kras-mutant B22 cells**	N/A	10 mg/mL	17.8 mg/mL	177.8 mg/mL
***In vivo* circulation time ($t_{1/2}$) (h)**	16.6±3.5	10.9±1.0	12.9±1.9	6.6±1.9
***In vivo* maximal tumor accumulation in SQ model (fold)**	2.4±0.7	2.1±0.4	N/A	3.9±0.7
***In vivo* maximal tumor accumulation in autochthonous model (fold)**	2.3±0.7	2.5±0.4	N/A	3.4±0.7